



ARTICLE

Thermo-Economic Performance Comparison between Basic Organic Rankine Cycle and Organic Rankine Cycle with Vapor-Liquid Ejector Driven by Solar Energy

Lingbao Wang^{1,2}, Zhi Gan², Zuowei Yang^{3,*}, Huashan Li^{1,2}, Yulie Gong^{1,2} and Xianbiao Bu^{1,2}

¹School of Energy Science and Engineering, University of Science and Technology of China, Guangzhou, 510640, China

²Guangzhou Institute of Energy Conversion, Chinese Academy of Sciences, Guangzhou, 510640, China

³Industrial Turbine Division, Dongfang Turbine Co., Ltd., Deyang, 618000, China

*Corresponding Author: Zuowei Yang. Email: yangzuowei@dongfang.com

Received: 24 October 2024; Accepted: 31 January 2025; Published: 31 March 2025

ABSTRACT: Amidst the global push for decarbonization, solar-powered Organic Rankine Cycle (SORC) systems are gaining significant attention. The small-scale Organic Rankine Cycle (ORC) systems have enhanced environmental adaptability, improved system flexibility, and achieved diversification of application scenarios. However, the power consumption ratio of the working fluid pump becomes significantly larger relative to the total power output of the system, adversely impacting overall system efficiency. This study introduces an innovative approach by incorporating a vapor-liquid ejector into the ORC system to reduce the pump work consumption within the ORC. The thermo-economic models for both the traditional ORC and an ORC integrated with a vapor-liquid ejector driven by solar parabolic trough collectors (PTCs) were developed. Key evaluation indicators, such as thermal efficiency, exergy efficiency, specific investment cost, and levelized cost of energy, were employed to compare the SORC with the solar ejector organic Rankine cycle (SEORC). Additionally, the study explores the effects of solar beam radiation intensity, PTC temperature variation, evaporator pinch point temperature difference, and condenser pinch point temperature difference on the thermo-economic performance of both systems. Results demonstrate that SEORC consistently outperforms SORC. Higher solar radiation intensity and increased PTC inlet temperature lead to better system efficiency. Moreover, there is an optimal PTC temperature drop where both thermal and exergy efficiencies are maximized. The influence of evaporator and condenser temperature pinches on system performance is found to be inconsistent.

KEYWORDS: Solar parabolic trough collector; organic Rankine cycle; vapor-liquid ejector; thermo-economic

1 Introduction

Global economic expansion and urbanization have resulted in severe environmental pollution and substantial CO₂ emissions [1]. In response to climate change, China has pledged to reach peak total CO₂ emissions before 2030 and achieve carbon neutrality before 2060, as announced on 22 September 2020, at the 75th United Nations (UN) General Assembly. To achieve this ambitious goal, the development of renewable and clean energy has become one of the most crucial strategies, garnering escalating attention [2]. Solar energy, with the abundance and widespread distribution, is supposed to a preferred solution to address the global climate change [3].



Organic Rankine cycle (ORC) is one of the most attractive technologies for harnessing solar energy [4]. Solar collectors capture solar radiation and convert it into heat. Among the various types of solar collectors, including flat-plate collectors with reflectors, parabolic trough collectors (PTCs), compound parabolic collectors, and Fresnel lens concentrating collectors, PTCs are the most commonly used for delivering process heat [5]. Over the past decades, extensive theoretical and experimental research has been conducted on PTC powered ORC systems. Rayegan et al. [6] developed a systematic approach for the selection of an appropriate working fluid. This method considers the molecular composition, their temperature-entropy characteristics, and the influence of these attributes on the thermodynamic efficiency of the system. Desai et al. [7] conducted thermo-economic investigation and working fluid selection for solar ORC. Soulis et al. [8] constructed a simulation model of a two-stage ORC engine coupled with evacuated tube solar collectors. The model was based on daily meteorological data covering a period of thirty-four years. The findings indicated significant spatial variability in the system's performance. Calise et al. [9] conducted a thermo-economic optimization analysis of the heat exchanger parameters and demonstrated the off-design operational characteristics of a PTC powered ORC system that utilizes butane as its working fluid. Rounpedakis et al. [10] executed an assessment that combined exergetic and economic evaluations of a compact solar-powered ORC system. Georoussis et al. [11] performed an optimization study with multiple objectives for a PTC-driven ORC system, employing CO₂ as the working fluid.

Research in PTC-ORC has predominantly focused on working fluid selection, operating parameters optimization, components geometrical parameter optimization, multi-objective optimization and off-design study. These studies aimed at improving the thermodynamic efficiency of PTC-ORC systems. Javed et al. [12] carried out a comparative evaluation of three distinct ORC setups, encompassing basic, recuperative, and regenerative types, assessing them from both energetic and financial viewpoints. The results demonstrate that the regenerative ORC configuration, utilizing Toluene as the working fluid, outperforms the other configurations. Freeman et al. [13] introduced a concept for a domestic-scale PTC-ORC system designed for cogeneration of power and heat, tailored for the UK's climate conditions. Bellos et al. [14] conducted a study focused on the investigation and enhancement of a trigeneration system designed for the concurrent generation of heating, cooling, and electricity. Jafary et al. [15] proposed and evaluated two distinct trigeneration system configurations driven by PTC, namely a regenerative ORC and an ORC system equipped with an internal heat exchanger.

The working fluid pump in ORC systems significantly impacts the overall system performance and stable operation. In the current literature on ORC systems, the efficiency of the working fluid pump is commonly estimated to range from 65% to 85% [16,17]. However, under current technological conditions, the actual operational efficiency of working fluid pumps frequently are less than these assumed values [18,19]. Zhang [20] emphasized that the selection of an appropriate circulation pump is pivotal to the system's performance, as an unsuitable pump can lead to negative efficiency when its power consumption is accounted for. Jiang et al. [21] addressed this issue by developing a small-scale pumpless ORC system, which innovatively eliminates the pump to reduce the significant electrical power consumption and thereby enhances system efficiency. Yang et al. [22] evaluated the performance of different types of working fluid pumps used in ORC systems. Their analysis showed that the efficiency rates for multistage centrifugal pumps, hydraulic diaphragm metering pumps, and roto-jet pumps are 58.76%, 55.26%, and 30.51%, respectively. These results highlight the significant influence that the efficiency of the working fluid pump has on the overall efficiency of the ORC system. Furthermore, the working fluid pumps power consumption remains relatively high in medium-scale ORC systems [23,24]. Therefore, investigating strategies to reduce the power consumption of ORC pumps is of practical significance.

As an alternative expansion mechanism, the ejector is widely utilized due to its simple design, absence of moving parts, easy operation, and low maintenance requirements. The integration of an ejector into an ORC can reduce working fluid pumps power consumption. Wang et al. [25] conducted a comprehensive comparison of configurations, components, and working fluid options for small-scale solar ORC systems. The assessments considered a variety of solar collector types, different power cycle configurations, a range of expander types along with their respective designs, and a selection of suitable working fluids. Haghparast et al. [26] conducted a parametric optimization and evaluated the performance of an ejector integrated into an ORC. Sanaye et al. [27] proposed an innovative configuration combining an ejector refrigeration cycle with an ORC system for transformer cooling and power generation. In all the studies, the vapor produced by the second-stage evaporator was employed as the primary fluid for the ejector. The significance of this study lies in its innovative approach to enhancing the efficiency of solar-powered Organic Rankine Cycle (SORC) systems by integrating a vapor-liquid ejector, which has the potential to significantly reduce working fluid pumps power consumption and improve overall system performance. In present paper, vapor-liquid ejector serves as the primary fluid to entrain liquid from the condenser. The vapor of the working fluid at intermediate pressure, which is extracted from the expander, serves as the principal medium to entrain the liquid from the condenser. The vapor-liquid ejector not only reduces turbine backpressure but also enhances the working fluid pump inlet pressure. Initially, a comprehensive thermo-economic model of the PTC-ORC with the vapor-liquid ejector (SEORC) is established. Subsequently, a comparative analysis from both thermal and economic perspectives between the solar ORC (SORC) and SEORC is conducted. Finally, an investigation was conducted to assess the impact of critical operational parameters on system performance.

2 System Description

Fig. 1 illustrates the schematic diagram and temperature-entropy (T-s) of the SORC, with an extensive system description available in reference [28]. Fig. 2 presents the schematic diagram and the temperature-entropy (T-s) of the SEORC. The system predominantly comprises a PTC collector array, an evaporator, a turbine, a condenser, an ejector, and a working fluid pump. Syltherm 800 serves as the thermal transfer fluid, which is initially heated in the PTC collector and then proceeds to the evaporator to bring the working fluid to a saturated state. Noted for its broad operational range and resistance to pipe clogging, is ideal for this application. The working fluid experiences three stages: preheating (8–9), evaporation (9–10), and superheating (10–1), transforming into superheated vapor prior to entering the turbine. A portion of the vapor is throttled to intermediate pressure (1–6) and directed to the ejector as the primary flow, while the remainder continues to expand, generating work. The turbine's exhaust is conveyed to the condenser, wherein the exhaust stream undergoes cooling and liquefaction facilitated by a precooling process using cooling water (2–3), condensation (3–4), and subcooling (4–5). The liquefied fluid then serves as the secondary flow for the ejector.

Fig. 3 illustrates schematic diagram of the ejector. The primary flow undergoes acceleration and expansion as it passes through the nozzle, resulting in the formation of a low-pressure zone at the inlet of the mixing chamber. Concurrently, the secondary flow is drawn into the mixing chamber by the action of vacuum and shear forces. Inside the mixing chamber, the primary flow condenses through direct contact heat transfer, leading to the formation of a uniform two-phase flow through vigorous mass, momentum, and heat exchange. At this stage, the two-phase flow is still supersonic and undergoes sudden compression, creating a strong condensation shock wave at the mixing chamber's end, rapidly increasing the fluid pressure. Finally, the mixed fluid's pressure rises further in the diffusion chamber, facilitating efficient heat transfer and pressurization. Following pressurization by the working fluid pump (7–8), the mixed fluid is channeled

back to the evaporator to continue the cycle. The selection of R245fa as the working fluid is attributed to its superior thermal characteristics and favorable environmental profile [29], with a comprehensive overview of its thermophysical properties detailed in Table 1. The fluid properties in the simulation are calculated using the CoolProp library [30].

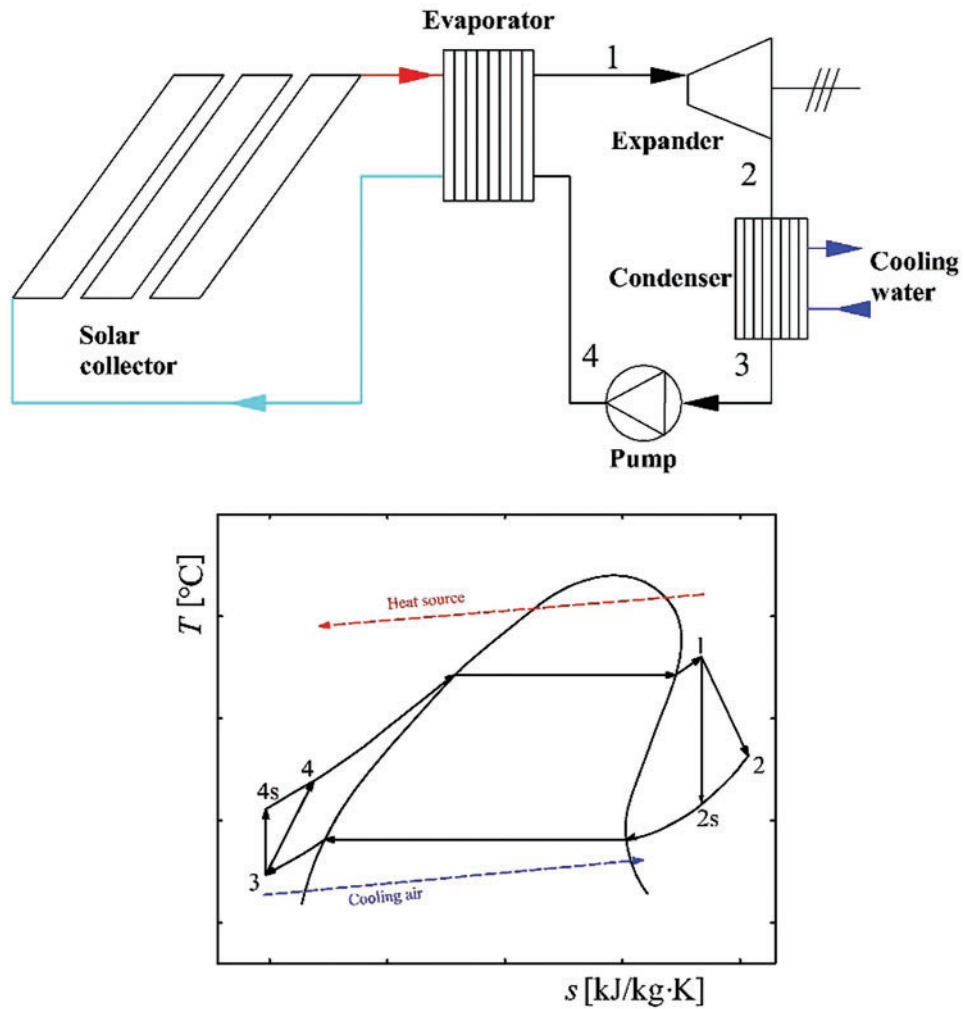


Figure 1: Schematic diagram and T-s chart of SORC

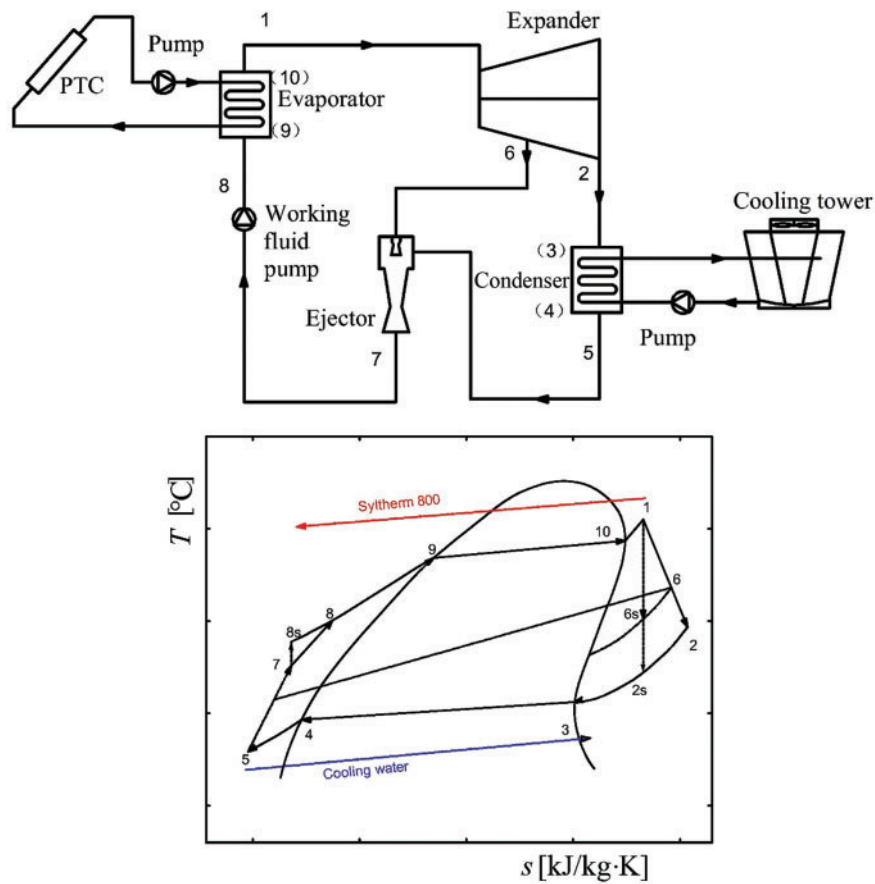


Figure 2: Schematic diagram and T-s chart of SEORC

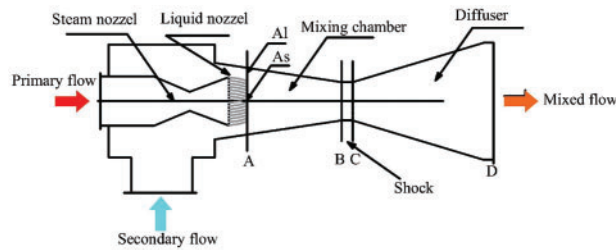


Figure 3: Schematic diagram of ejector

Table 1: Thermophysical characteristics of R245fa

Fluid	Mole mass (g/mol)	Normal boiling point (°C)	Critical temperature (°C)	Critical pressure (kPa)	Flammability	ODP	GWP
R245fa	134.05	15.1	154.0	3650	Non-flammable	0	1030

3 System Model

3.1 Thermodynamic Assumptions

The following assumptions are made to simplify the analysis of SEORC:

- (1) The system is modeled under steady-state conditions;
- (2) Pressure and heat losses are neglected for all components, except in the turbine and pump;
- (3) Friction losses, as well as the kinetic energy and potential energy of operating process are ignored;
- (4) The incidence angle and surface temperature are assumed to zero and 5770 K;
- (5) The ambient temperature and pressure are assumed to be 25°C and 101.325 kPa, respectively;
- (6) The primary and secondary fluids are supplied to the ejector under stagnation state;
- (7) The fluid at the exit of ejector is under stagnation state.

3.2 Thermodynamic Model

The available energy from the sun can be calculated by

$$Q_{\text{ava}} = A_{\text{col}} G_{\text{b}} \quad (1)$$

where Q represents the heat transfer rate, kW; A is the area, m^2 ; G_{b} indicates the solar beam radiation intensity, W/m^2 . The subscript “ava” denotes available.

The PTC’s thermal efficiency is determined by [31,32]

$$\eta_{\text{col}} = 0.762 - 0.215 \left(\frac{T_{\text{ave}} - T_0}{G_{\text{b}}} \right) - 0.001672 \left(\frac{T_{\text{ave}} - T_0}{G_{\text{b}}} \right)^2 \quad (2)$$

$$T_{\text{ave}} = \frac{T_{\text{col,in}} + T_{\text{col,out}}}{2} \quad (3)$$

where η signifies the thermal efficiency; T is temperature, °C. The subscripts “col”, “ave”, “am”, “in” and “out” denote the PTC, average, ambient, inlet and outlet, respectively.

The evaporator’s available energy is given by

$$Q_{\text{use}} = Q_{\text{ava}} \eta_{\text{col}} \quad (4)$$

The mass flow rate of Syltherm 800 in the PTC is expressed as

$$m_{\text{syl}} = \frac{Q_{\text{use}}}{C_{\text{p,syl}} (T_{\text{col,in}} - T_{\text{col,out}})} \quad (5)$$

where m represents the mass flow rate, kg/s; C_{p} represents the specific heat capacity, $\text{kJ}/(\text{kg}\cdot\text{K})$; T represents the temperature, °C; h represents the specific enthalpy, kJ/kg ; the subscripts “syl” and “col” denote the syltherm 800 and solar collector, respectively.

The PTC’s input exergy is given by

$$E_{\text{col,in}} = m_{\text{syl}} \left((h_{\text{col,in}} - h_{0,\text{syl}}) - T_0 (s_{\text{col,in}} - s_{0,\text{syl}}) \right) \quad (6)$$

The PTC’s output exergy is given by

$$E_{\text{col,out}} = m_{\text{syl}} \left((h_{\text{col,out}} - h_{0,\text{syl}}) - T_0 (s_{\text{col,out}} - s_{0,\text{syl}}) \right) \quad (7)$$

where E is the available solar exergy, kW.

The exergy obtained by the solar radiation is given by

$$E_{\text{sol,in}} = A_{\text{col}} I_b \left(1 - \frac{3}{4} \frac{T_0}{T_{\text{sol}}} + \frac{1}{3} \frac{T_0^4}{T_{\text{sol}}^4} \right) \quad (8)$$

The PTC's exergy efficiency is given by

$$\eta_{\text{ex,col}} = \frac{E_{\text{col,out}} - E_{\text{col,in}}}{E_{\text{sol,in}}} \quad (9)$$

where the subscript "ex" denotes exergy.

Vapor-liquid ejector model

Vapor-liquid ejectors are characterized by their ability to produce an outlet pressure that exceeds the primary flow pressure. Consequently, this feature can lead to a reduction in the working fluid pump power consumption, and it allows for the anticipation of a more substantial net power output. The ejector features a central steam nozzle design. It is composed of three distinct sections: an intake section for drawing in the secondary fluid, a mixing chamber where the primary and secondary flows combine, and a diffuser that facilitates the pressure increase and flow transformation.

Steam nozzle

At the outlet of steam nozzle (section A_s), the pressure of primary flow is low, and the velocity is supersonic.

The primary flow pressure at section A_s is expressed as

$$p_{A_s} = p_s \cdot \varepsilon \quad (10)$$

where p_s is the initial pressure of the primary flow, kPa; p_{A_s} is the primary flow pressure at section A , kPa; ε is the expansion rate assumed to be 0.25 [33].

The primary flow enthalpy at section A_s is expressed as

$$h_{A_s} = h_s - \eta_{n,s} (h_s - h_{A_s,s}) \quad (11)$$

where h_{A_s} is the primary flow enthalpy, kJ/kg; h_s represents the initial enthalpy of the primary flow, kJ/kg; $h_{A_s,s}$ denotes the primary flow enthalpy during the isentropic process, kJ/kg; $\eta_{n,s}$ is the steam nozzle's isentropic efficiency.

The primary flow velocity at section A_s is given by

$$u_{A_s} = \sqrt{2(h_s - h_{A_s})} \quad (12)$$

where u_{A_s} is velocity A_s , m/s.

The sectional area of section A_s is given by

$$A_{A_s} = m_s / (\rho_{A_s} \cdot u_{A_s}) \quad (13)$$

where A_{A_s} is the area, m^2 ; m_s is the primary flow's mass flow rate, kg/s; ρ_{A_s} is the density, kg/m^3 .

Liquid nozzle

The secondary flow pressure at the outlet of liquid nozzle (section A_1) is given by

$$p_{A1} = p_{As} \quad (14)$$

where p_{A1} is the secondary flow pressure, kPa.

The secondary flow enthalpy at section A_1 is given by

$$h_{A1} = h_1 - \eta_{n,l} (h_1 - h_{A1,s}) \quad (15)$$

where h_{A1} is the secondary flow enthalpy, kJ/kg; h_1 denotes the initial enthalpy of the secondary flow, kJ/kg; $h_{A1,s}$ represents the secondary flow enthalpy at section A_s during the isentropic process, kJ/kg; $\eta_{n,l}$ is the liquid nozzle's isentropic efficiency taken as 0.85 [34].

The secondary flow velocity at section A_1 is given by

$$u_{A1} = \sqrt{2(h_1 - h_{A1})} \quad (16)$$

where u_{A1} is the secondary flow velocity at section A_1 , m/s.

The sectional area of section A_1 is given by

$$A_{A1} = m_1 / (\rho_{A1} \cdot u_{A1}) \quad (17)$$

where A_{A1} is the area, m^2 ; m_1 is the secondary flow's mass flow rate, kg/s; ρ_{A1} is the secondary flow density at section A_1 , kg/m^3 .

Mixing chamber before shock

The mixing chamber serves as the crucial component within the ejector, where the exchange of mass, momentum, and heat occurs between the vaporous and liquid phases of the working fluid.

The area of section B is given by

$$A_B = A_{As} R_{A,B} \quad (18)$$

where A_B is the area of section B , m^2 ; $R_{A,B}$ is the section area ratio assumed to be 0.36.

The mass flow rate of section B is given by

$$m_B = m_1 + m_s \quad (19)$$

where m_B is the mixed working fluid's mass flow rate, kg/s.

The mixed working fluid's velocity is given by [35]

$$u_b = \frac{(u_{As} + \mu \cdot u_{A1}) \sqrt{\eta_{mix}}}{1 + \mu} \quad (20)$$

where μ is the entrainment ratio; η_{mix} is the mixing efficiency estimated at 0.95.

The mixed working fluid's enthalpy at section B is given by

$$h_B = \frac{(h_s + \mu \cdot h_1)}{1 + \mu} - \frac{u_B^2}{2} \quad (21)$$

The mixed working fluid's density at section B is given by

$$\rho_B = m_B / (A_B \cdot u_B) \quad (22)$$

The mixed working fluid's fraction dryness at section B is given by

$$VF = \frac{x_B \rho_l}{x_B \rho_l + (1 - x_B) \rho_s} \quad (23)$$

where F denotes mixed working fluid's fraction dryness, %; x is the dryness; ρ_l is the density of liquid-state part of the mixed working fluid, kg/m^3 ; ρ_s is the density of steam-state part of the mixed working fluid, kg/m^3 .

The mixed working fluid's sound velocity is given by

$$u_{\text{sonic,m}} = \frac{1}{\sqrt{\left(\frac{VF}{\rho_s \cdot c_s^2} + \frac{(1-VF)}{\rho_l \cdot c_l^2} \right) \rho_B}} \quad (24)$$

where $u_{\text{sonic,m}}$ is the sound velocity, m/s; c_s is the sound velocity of steam-state part of the mixed working fluid, m/s; c_l is the sound velocity of liquid-state part of the mixed working fluid, m/s.

The Mach number at section B is given by

$$Ma_B = u_B / u_{\text{sonic,m}} \quad (25)$$

where Ma_B is the Mach number at section B .

The Mach number at section C is given by

$$Ma_C = \sqrt{\frac{Ma_B^2 + 2 / (k - 1)}{2kMa_B^2 / (k - 1) - 1}} \quad (26)$$

where Ma_C is The Mach number at section C ; k is heat capacity ratio.

The pressure at section C is given by

$$p_C = p_B \frac{1 + kMa_B^2}{1 + kMa_C^2} \quad (27)$$

The velocity at section C is given by

$$u_C = (m_B u_B + p_B A_B - p_C A_C) / m_C \quad (28)$$

The enthalpy at section C is given by

$$h_C = \frac{\left(\rho_B u_B \left(h_B + \frac{u_B^2}{2} \right) \right)}{\rho_C u_C} - \frac{u_C^2}{2} \quad (29)$$

Diffuser

The pressure at section D is given by [36]

$$p_D = p_D + \eta_{\text{diff}} \left(\rho_C \frac{u_C^2}{2} \right) \quad (30)$$

where η_{diff} is the diffuser efficiency assumed to be 0.65.

The evaporator

The evaporator is the bridge between the PTC sub-system and the ORC sub-system. The energy conservation within the evaporator is described by

$$Q_e = m_{\text{syl}} (h_{\text{col,out}} - h_{\text{col,in}}) = m_{\text{wf}} (h_1 - h_8) \quad (31)$$

where m denotes the mass flow rate, kg/s; h denotes the specific enthalpy, kJ/kg; the subscripts “syl” and “wf” correspond to the syltherm 800 and working fluid, respectively. The numerical subscripts in these equations match those shown in Fig. 2.

The evaporator's entropy generation is given by

$$S_{\text{gen,e}} = m_{\text{wf}} (s_1 - s_8) + m_{\text{syl}} (s_{\text{col,in}} - s_{\text{col,out}}) \quad (32)$$

where $S_{\text{gen,e}}$ is the entropy generation, kW/K.

The evaporator's entropy generation is given by

$$I_e = T_0 \cdot S_{\text{gen,e}} \quad (33)$$

where I_e is the irreversible loss of the evaporator, kW.

The evaporator is structured into three distinct segments, namely preheating section, evaporation section and superheating section.

The thermal conductivity rate of the preheating section is given by

$$KA_{e1} = \frac{m_{\text{wf}} (h_9 - h_8)}{(T_{\text{col,in}} - T_8 - \Delta t_{\text{pp}}) / \ln((T_{\text{col,in}} - T_8) / \Delta t_{\text{pp}})} \quad (34)$$

where KA_{e1} is thermal conductivity rate of the preheating section, $W/^\circ\text{C}$; Δt_{pp} is the pinch point difference, $^\circ\text{C}$.

The thermal conductivity rate of the evaporation section is given by

$$KA_{e2} = \frac{m_{\text{wf}} (h_{10} - h_9)}{(T_{\text{syl},1} - T_{10} - \Delta t_{\text{pp}}) / \ln((T_{\text{syl},1} - T_{10}) / \Delta t_{\text{pp}})} \quad (35)$$

where KA_{e2} is thermal conductivity rate of the evaporation section, $W/^\circ\text{C}$.

The thermal conductivity rate of the superheating section is given by

$$KA_{e3} = \frac{m_{\text{wf}} (h_1 - h_{10})}{(T_{\text{col,out}} - T_1) - (T_{\text{syl},1} - T_{10}) / \ln((T_{\text{col,out}} - T_1) / (T_{\text{syl},1} - T_{10}))} \quad (36)$$

where KA_{e3} is thermal conductivity rate of the superheating section, $W/^\circ\text{C}$.

The Chisholm & Wanniarachchi correlation [37] is applied to determine the single-phase convective heat transfer coefficient for R245fa and water within the evaporator.

$$\frac{KD_h}{\lambda} = 0.72 \left(\frac{90 - \beta}{\pi} \right)^{0.66} Re^{0.59} Pr^{0.4} \phi^{0.41} \quad (37)$$

where d_h denotes the hydraulic diameter, m; λ denotes coefficient of thermal conductivity, W/(m·K); β denotes the corrugation angle on the surface of a plate; Re denotes the Reynolds number; Pr denotes Prandtl number; ϕ denotes enlargement factor.

$$Pr = \frac{C_p \eta}{\lambda} \quad (38)$$

where C_p denotes the specific heat capacity, kJ/(kg·K); η denotes the viscosity, Pa·s.

$$\phi = \frac{1}{6} \left(1 + \sqrt{1 + \left(\frac{\pi b}{p_{co}} \right)} + 4 \sqrt{1 + \frac{1}{2} \left(\frac{\pi b}{p_{co}} \right)} \right) \quad (39)$$

where b is corrugation height, m; p_{co} is corrugation pitch, m.

$$Re = \frac{G d_h}{\eta} \quad (40)$$

where G denotes the mass velocity kg/(m²·s).

$$d_h = 2b \quad (41)$$

$$G = \frac{m_{wf}}{b W N} \quad (42)$$

where WN is plate width, m.

Han correlation [38] is used to calculate the two-phase flow boiling heat transfer coefficient of R245fa in the evaporator.

$$\frac{KD_h}{\lambda} = Ge_1 Re_e^{Ge_2} Bo_e^{0.3} Pr^{0.4} \quad (43)$$

where Re_{eq} denotes the equivalent Reynolds number, and Bo_{eq} denotes the equivalent boiling number.

$$Ge_1 = 2.81 \left(\frac{p_{co}}{D_h} \right)^{-0.041} \left(\frac{\pi}{2} - \beta \right)^{-2.83} \quad (44)$$

$$Ge_2 = 0.746 \left(\frac{p_{co}}{D_h} \right)^{-0.082} \left(\frac{\pi}{2} - \beta \right)^{0.61} \quad (45)$$

where Ge_1 and Ge_2 are non-dimensional geometric parameters, respectively.

$$Re_e = \frac{G_e d_h}{\eta} \quad (46)$$

$$Bo_e = \frac{q}{G_e h_{fg}} \quad (47)$$

$$Ge = G \left[1 - x_m + x_m \left(\frac{\rho_l}{\rho_v} \right)^{0.5} \right] \quad (48)$$

where x_m denotes the vapor quality.

The power output of the turbine is given by

$$W_t = m_1 (h_1 - h_2) + m_s (h_1 - h_6) = (m_1 (h_1 - h_{2,s}) + m_s (h_1 - h_{6,s})) \eta_t \quad (49)$$

where W denotes the power, kW; η_t denotes the turbine's isentropic efficiency.

The turbine's entropy generation is given by

$$S_{\text{gen},t} = m_{\text{wf}2} (s_2 - s_1) + m_{\text{wf}6} (s_6 - s_1) \quad (50)$$

The turbine's irreversible loss is given by

$$I_t = T_0 \cdot S_{\text{gen},t} \quad (51)$$

The thermal energy exchanged within the condenser is given by

$$Q_c = m_{\text{cw}} (h_{\text{cw},\text{out}} - h_{\text{cw},\text{in}}) = m_{\text{wf}} (h_2 - h_5) \quad (52)$$

The entropy generation of the condenser is given by

$$S_{\text{gen},c} = m_{\text{cw}} (s_{\text{cw},\text{out}} - s_{\text{cw},\text{in}}) + m_{\text{wf}} (s_5 - s_2) \quad (53)$$

The irreversible loss of the condenser is given by

$$I_c = T_0 \cdot S_{\text{gen},c} \quad (54)$$

The condenser is structured into three distinct segments, namely precooling section, condensation section and subcooling section.

The thermal conductivity rate of the precooling section is given by

$$KA_{c1} = \frac{m_{\text{wf}2} (h_2 - h_3)}{((T_2 - T_{\text{cw},\text{out}}) - (T_3 - T_{\text{cw},2})) / \ln((T_2 - T_{\text{cw},\text{out}}) / (T_3 - T_{\text{cw},2}))} \quad (55)$$

where KA_{c1} is thermal conductivity rate of the precooling section, $W/^\circ\text{C}$.

The thermal conductivity rate of the condensation section is given by

$$KA_{c2} = \frac{m_{\text{wf}2} (h_3 - h_4)}{((T_4 - T_{\text{cw},1}) - (T_3 - T_{\text{cw},2})) / \ln((T_4 - T_{\text{cw},1}) / (T_3 - T_{\text{cw},2}))} \quad (56)$$

where KA_{c2} is thermal conductivity rate of the condensation section, $W/^\circ\text{C}$.

The thermal conductivity rate of the subcooling section is given by

$$KA_{c3} = \frac{m_{\text{wf}2} (h_4 - h_5)}{((T_4 - T_{\text{cw},1}) - (T_5 - T_{\text{cw},\text{in}})) / \ln((T_4 - T_{\text{cw},1}) / (T_5 - T_{\text{cw},\text{in}}))} \quad (57)$$

where KA_{c3} is thermal conductivity rate of the condensation section, $W/^\circ\text{C}$.

Eqs. (37)–(42) are used to calculate the single-phase heat transfer coefficient of R245fa and water in the condenser.

Longo correlation [39] is used to calculate the two-phase flow condensation heat transfer coefficient of R245fa in condenser.

If $Re < 1600$

$$K = 0.943\varphi \left[\frac{\lambda^3 \rho_3 g h_{fg}}{\lambda (T_{wf} - T_{wall})} \right]^{0.25} \quad (58)$$

If $Re \geq 1600$

$$K = 1.875 \frac{\lambda}{D_h} Re_e^{0.445} Pr^{1/3} \quad (59)$$

The pump consumed power is expressed as

$$W_p = m_{wf7} (h_8 - h_7) = m_{wf7} (h_{8,s} - h_7) / \eta_p \quad (60)$$

The pump entropy generation is expressed as

$$S_{gen,p} = m_{wf7} (s_8 - s_7) \quad (61)$$

The pump irreversible loss is expressed as

$$I_p = T_0 \cdot S_{gen,p} \quad (62)$$

The gross power output is expressed as

$$W_{net} = \eta_m \eta_g W_t - W_p \quad (63)$$

The EORC's thermal efficiency is expressed as

$$\eta_{th,EORC} = W_{net} / Q_e \quad (64)$$

The SEORC's thermal efficiency is expressed as

$$\eta_{th} = \eta_{col} \eta_{th,EORC} \quad (65)$$

The EORC's exergy efficiency is expressed as

$$\eta_{ex,EORC} = W_{net} / (E_{col,out} - E_{col,in}) \quad (66)$$

The SEORC's exergy efficiency is expressed as

$$\eta_{ex} = \eta_{ex,col} \eta_{ex,EORC} \quad (67)$$

The PTC investment cost is given by

$$C_{col} = 120 A_{col} \quad (68)$$

In the SEORC system, a modular costing method is adopted to calculate the fundamental cost of each component, whereas the current capital expenditure is assessed using the Chemical Engineering Plant Cost Index (CEPCI).

The heat exchanger investment cost is given by

$$C_{hx} = \frac{CEPCI_{2022}}{CEPCI_{2001}} F_s C_{hx}^0 (B_{1,hx} + B_{2,hx} F_{m,hx} F_{p,hx}) \quad (69)$$

where C_{hx} represents the heat exchanger investment cost, \$; $CEPCI_{2001}$ and $CEPCI_{2022}$ represent the chemical engineering plant cost index of 2001 and 2022, respectively; F_s is additional factor; C_{hx}^0 is the basic investment cost, \$; $B_{1,hx}$ and $B_{2,hx}$ denote the constant values.; $F_{m,hx}$ and $F_{p,hx}$ are the material and pressure factor, respectively.

$$\log C_{hx}^0 = K_{1,hx} + K_{2,hx} \log A_{hx} + K_{3,hx} (\log A_{hx})^2 \quad (70)$$

$$\log F_{p,hx} = C_{1,hx} + C_{2,hx} \log P_{hx} + C_{3,hx} (\log P_{hx})^2 \quad (71)$$

where $K_{1,hx}$, $K_{2,hx}$, $C_{1,hx}$, $C_{2,hx}$ and $C_{3,hx}$ denote the constant values; A_{hx} represents the area of the plate-type heat exchanger, m^2 ; P_{hx} denotes the design pressure for a plate-type heat exchanger, bar.

The working fluid pump investment cost is given by

$$C_{pp} = \frac{CEPCI_{2022}}{CEPCI_{2001}} F_s C_{pp}^0 (B_{1,pp} + B_{2,pp} F_{m,pp} F_{p,pp}) \quad (72)$$

where C_{pp} is the pump investment cost, \$; $F_{m,pp}$ and $F_{p,pp}$ are additional factor and pressure factor, respectively; C_{pp}^0 denotes the basic cost, \$.

$$\log C_{pp}^0 = K_{1,pp} + K_{2,pp} \log W_{pp} + K_{3,pp} (\log W_{pp})^2 \quad (73)$$

$$\log F_{p,pp} = C_{1,pp} + C_{2,pp} \log P_{pp} + C_{3,pp} (\log W_{pp})^2 \quad (74)$$

where $B_{1,pp}$, $B_{2,pp}$, $K_{1,pp}$, $K_{2,pp}$, $K_{3,pp}$, $C_{1,pp}$, $C_{2,pp}$ and $C_{3,pp}$ denote the constant values; P_{pp} represents the pressure, bar; W_{pp} denotes power consumption, kW.

The turbine investment cost is given by

$$C_t = \frac{CEPCI_{2022}}{CEPCI_{2001}} F_s C_t^0 F_{m,t} \quad (75)$$

$$\log C_t^0 = K_{1,t} + K_{2,t} \log W_t + K_{3,t} (\log W_t)^2 \quad (76)$$

where C_t is turbine investment cost, \$; $F_{m,t}$ denotes the pressure factor; C_t^0 represents the basic cost; $K_{1,t}$, $K_{2,t}$ and $K_{3,t}$ are designated as constants.

Note that the costs of the ejector, valve, pipe and working fluid are ignored in present study, since their costs are much lower than those of other components [40]. Furthermore, the overall investment is comprised of additional costs and miscellaneous expenses, which are estimated at 15% and 3% of the initial investment cost, respectively [41].

$$C_{tot} = 1.18 (C_{hx} + C_{pp} + C_t + C_{col}) \quad (77)$$

The specific investment cost is given by

$$SIC = \frac{C_{tot}}{W_{net}} \quad (78)$$

The capital recovery factor is expressed as [42]

$$CRF = \frac{i(1+i)^{LT}}{(1+i)^{LT} - 1} \quad (79)$$

With the interest rate (i) set at 5% and the operational lifetime (LT) at 20 years, the levelized cost of energy is calculated as follows:

$$LCOE = \frac{CRFC_{tot} + C_{om}}{W_{net}t_{op}} \quad (80)$$

where C_{om} represents the annual operation and maintenance cost, which is calculated at a rate of 1% of the total investment cost; t_{op} denotes the annual sunshine duration, estimated at 2500 h [43]. A comprehensive list of the parameters essential for the economic model is provided in Table 2, which enumerates the input parameters for the economic assessment.

Table 2: The key input parameters utilized in the economic model

Parameters	Value	Parameters	Value
CEPCI ₂₀₀₁	397	$C_{3,hx}$	0.00
CEPCI ₂₀₂₂	816.2	$F_{m,pp}$	1.50
i	5%	$K_{1,pp}$	3.389
LT	20	$K_{2,pp}$	0.0536
t_{op}	2500	$B_{1,pp}$	1.89
F_s	1.00	$B_{2,pp}$	1.35
$B_{1,hx}$	0.9600	$C_{1,pp}$	-0.3935
$B_{2,hx}$	1.2100	$C_{2,pp}$	0.3957
$F_{m,hx}$	1.0000	$C_{3,pp}$	-0.00226
$K_{1,hx}$	4.6656	$F_{m,exp}$	3.50
$K_{2,hx}$	-0.1557	$K_{1,exp}$	2.2476
$K_{3,hx}$	0.1547	$K_{2,exp}$	1.4965
$C_{1,hx}$	0.00	$K_{3,exp}$	-0.1618
$C_{2,hx}$	0.00	$K_{3,pp}$	0.1538

4 Model Validation

4.1 Model Validation of ORC

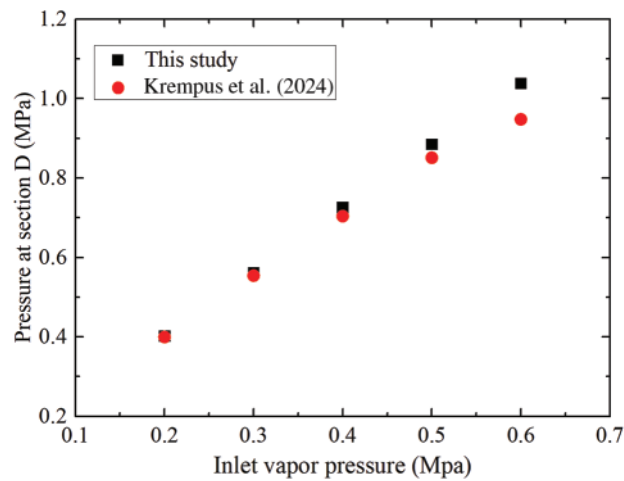
To evaluate the accuracy of the mathematical model developed for the ORC system in this research, a comparison was made between our findings and the data reported in the literature [44], under the same operational parameters as specified in Table 3. Our study's net output power, at 270.6 kW, shows a mere 0.22% increase from the 270 kW reported in the literature. Similarly, our thermal efficiency of 3.93% is only a 0.76% reduction compared to the 3.96% efficiency documented in the literature. These results demonstrate that the thermodynamic model used in present study is sufficiently accurate for the investigation of ORC system cycle characteristics.

Table 3: Comparison results with the ORC system in literature

Working fluid	Inlet temperature of hot water (°C)	Outlet temperature of hot water (°C)	Mass flow rate of hot water (kg/s)	Inlet temperature of cooling water (°C)	Outlet temperature of cooling water (°C)	Mass flow rate of cooling water (kg/s)	Net power output (kW)	Thermal efficiency (%)	
R123	91.1	73.3	69.44	28	38	162.5	270	3.96	Ref. [44]
R123	91.1	73.3	69.44	28	38	162.5	270.6	3.93	This study

4.2 Model Validation of Injector Model

Utilizing the identical parameters from Yan et al.'s experiments as referenced in [33], this study's injector model calculations were validated against the findings reported in the paper. Fig. 4 illustrates the model's calculated outcomes in relation to the empirical data, with the relative error spanning from 0.227% to 11.75%, predominantly under 10%. This range of error suggests that the injector model possesses a degree of precision and dependability.

**Figure 4:** Injector model validation [45]

5 Results and Discussions

5.1 Effects of Solar Beam Radiation Intensity

Utilizing the model previously established, a comparative thermo-economic analysis of the SORC and SEORC systems has been conducted. Comprehensive details regarding the input parameters and boundary conditions are provided in Table 4. Furthermore, the effects of solar beam radiation intensity on the performance of both the SORC and SEORC systems are illustrated in Figs. 5 and 6.

Table 4: Input parameters of economic model

Parameters	Symbols	Typical values	Ranges
Net power output (kW)	W_{net}	100	/
PTC outlet temperature ($^{\circ}\text{C}$)	$T_{col,out}$	140	130–165
Solar beam radiation intensity (W/m^2)	G_b	800	600–1000
PTC temperature drop ($^{\circ}\text{C}$)	ΔT	40	20–60
Evaporator pinch point temperature difference	PP_{eva}	5	3–15
Condenser Pinch point temperature difference	PP_{con}	5	3–15
Cooling water inlet temperature ($^{\circ}\text{C}$)	$T_{cw,in}$	20	/
Turbine's isentropic efficiency	η_{tur}	0.80	/
Work fluid pump's isentropic efficiency	η_{pup}	0.85	/
Ambient temperature ($^{\circ}\text{C}$)	T_{am}	25	/
Temperature of sun (K)	T_{sun}	5770	/

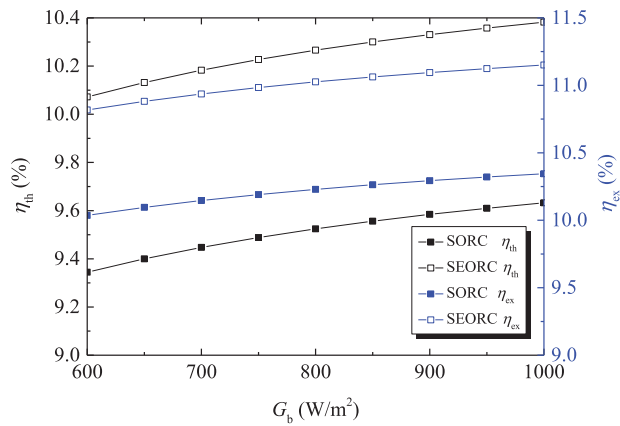


Figure 5: Variations of thermal efficiency and exergy efficiency with solar beam radiation intensity

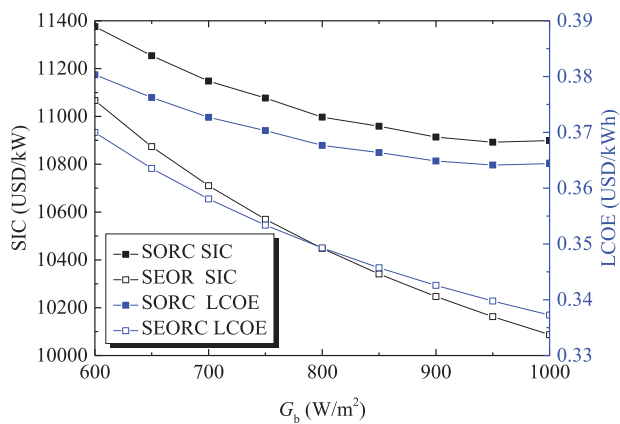


Figure 6: Variations of SIC and LCOE with solar beam radiation intensity

As observed in Fig. 3, it is anticipated that for the SORC and SEORC, a rise in solar beam radiation intensity leads to an increase in η_{th} and η_{ex} . Within the operational parameters examined, the solar beam radiation intensity has no impact on the thermal efficiency and exergy efficiency for the ORC and EORC systems. Nevertheless, a higher solar beam radiation intensity is beneficial for improving the PTC efficiency. The η_{th} and η_{ex} of SEORC surpass those of the SORC. This is attributed to the presence of the vapor-liquid ejector, which, on one hand, reduces the working fluid pump power consumption by decreasing the mass flow rate and increasing the pump's inlet pressure, and on the other hand, lowers the turbine backpressure, leading to an increase in the specific enthalpy drop across the turbine. Consequently, higher thermal and exergy efficiencies are anticipated. The working fluid pump's isentropic efficiency is assumed to be 0.85, which is significantly higher than the typical values observed in small-scale ORC systems [45]. That is to say the SEORC is more superior more than the SORC in the actual application. At a solar beam radiation intensity of 1000W/m^2 , the SEORC's thermal efficiency and exergy efficiency are 1.08 and 1.08 times as large as those of the SORC. As can be seen from Fig. 4, both the *SIC* and *LCOE* of the SORC and SEORC are decreased with the rising solar beam radiation intensity. Moreover, the solar beam radiation intensity has a more pronounced effect on the SORC, indicating that the SEORC is better suited for regions with lower solar beam radiation intensities.

5.2 Effects of PTC Temperature Drop

The influences of PTC temperature drop on the SORC and SEORC system performance are illustrated in Figs. 7 and 8. As observed in Fig. 6, with the rised ΔT , the η_{th} and η_{ex} initially show a slight increase followed by a decline. Given the designed heat exchanger pinch point temperature difference, net power output, and PTC inlet temperature, a higher ΔT delivers more heat to the evaporator, leading to a reduction in evaporation temperature. Consequently, the thermal efficiency of the ORC system is diminished. According to Eq. (1), the PTC efficiency increases with the incrising of ΔT . The interplay of these factors accounts for the variation in η_{th} and η_{ex} . An optimal ΔT exists at which both η_{th} and η_{ex} are maximized. Across all investigated ΔT values, the efficiencies of SEORC surpass those of SORC. Under higher ΔT conditions, SEORC demonstrates greater superiority over ORC. When the ΔT reaches 50°C , the η_{th} of SEORC is 1.17 times larger than that of ORC. From Fig. 7, the SEORC yields better economic performance. For ΔT values below 20°C , the economic performance of SORC and SEORC is comparable. At a ΔT of 50°C , the *SIC* and *LCOE* for SEORC experience a 6.3% reduction compared to SORC.

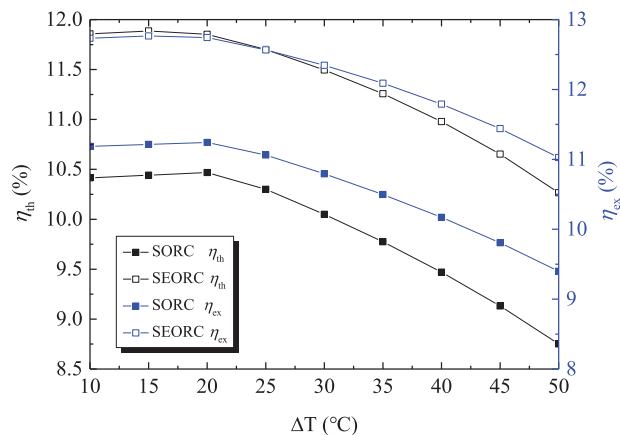


Figure 7: Variations of thermal efficiency and exergy efficiency with PTC temperature drop

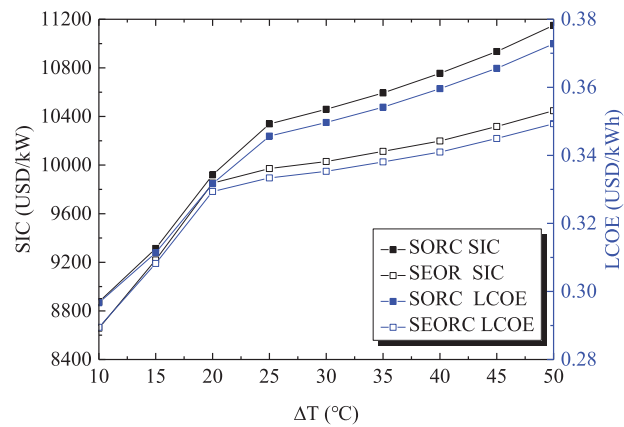


Figure 8: Variations of *SIC* and *LCOE* with PTC temperature drop

5.3 Effects of PTC Inlet Temperature

The influences of T_{in} on the SORC and SEORC system performance are depicted in Figs. 9 and 10. It is evident that for both systems, for the SORC and SEORC, Both the η_{th} and η_{ex} exhibit an increasing trend in response to an increase in T_{in} . Under the typical working conditions, the PTC efficiency declines with a rise in T_{in} . Obviously, higher T_{in} is conducive to the evaporation temperature rising, leading to the improvement of ORC and EORC thermal efficiency and exergy efficiency. Nevertheless, the increments in the thermal and exergetic efficiencies of both ORC and EORC systems exceed the decrease in PTC efficiency. Due to the synergistic influence of these two factors, η_{th} and η_{ex} of ORC and EORC both are increased. For SORC and SEORC, both the *SIC* and *LCOE* exhibit a downward trend as the T_{in} increases. With the net power output remains constant, higher values of T_{in} necessitate a reduction in the required heat exchanger and PTC areas. Notably, the efficiencies of SEORC consistently surpass those of SORC. As T_{in} increases, the ratio of SEORC's η_{th} to SORC's η_{th} ascends linearly. At a T_{in} of 165°C, the η_{th} of SEORC is 20% greater than that of SORC. In terms of economic performance, T_{in} exerts a more pronounced effect on the thermodynamic performance.

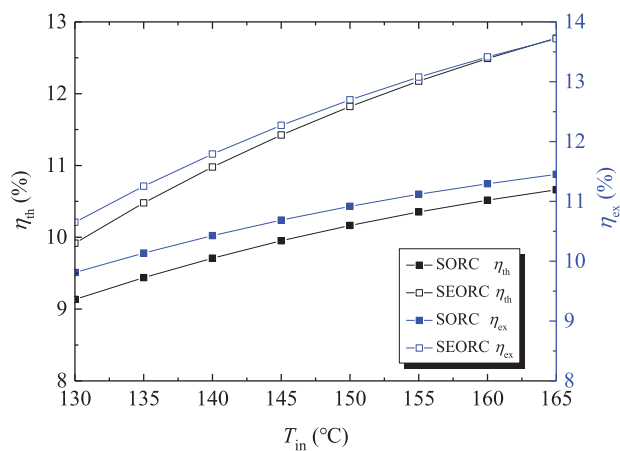


Figure 9: Variations of thermal efficiency and exergy efficiency with PTC inlet temperature

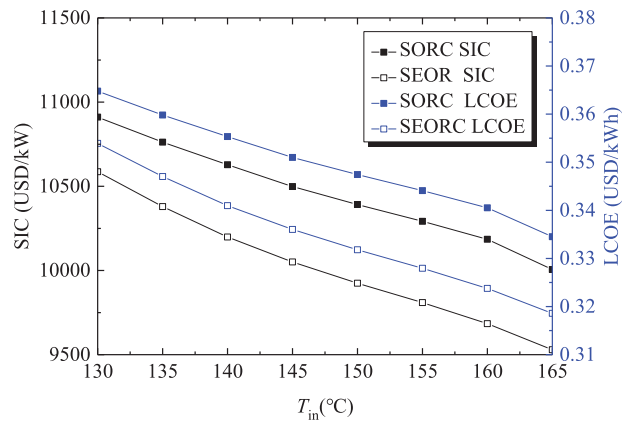


Figure 10: Variations of SIC and LCOE with PTC inlet temperature

5.4 Effects of Evaporator Pinch Point Temperature Difference

The influences of PP_{eva} on the on the SORC and SEORC system performance are depicted in Figs. 11 and 12. It is observable that an increase in PP_{eva} leads to a decline in both η_{th} and η_{ex} are decreased. Under the working condition investigated, the improvement of PP_{eva} has no impact on the PTC efficiency, but will lead to an decrease in the evaporation temperature, which causes the decreasing of the η_{th} and η_{ex} . The PP_{eva} has larger impact on the η_{th} and η_{ex} of SEORC than those of SORC. The increased PP_{eva} also causes the decreasing of the SIC and LCOE with decreased reduction rate. Given a set net power output, the decreased η_{th} necessitates a greater heat input into the evaporator. Based on the energy balance within the evaporator, the area required is dependent on both the PP_{eva} and the total heat input. The dual effect on the heat exchanger area accounts for the fluctuations in SIC and LCOE. When PP_{eva} exceeds 12°C , its influence on SIC and LCOE becomes marginal. That is to say the PP_{eva} should not surpass 12°C under the working conditions in this study. It is evident that it is not viable to achieve maximum thermodynamic performance (η_{th} and η_{ex}) and minimum economic performance (SIC and LCOE), simultaneously.

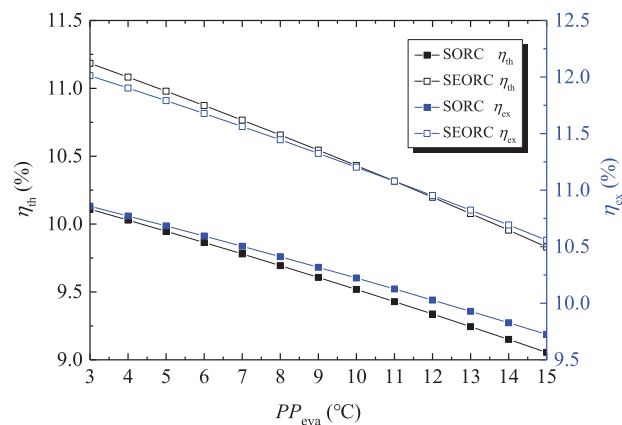


Figure 11: Variations of thermal efficiency and exergy efficiency with evaporator pinch point temperature difference

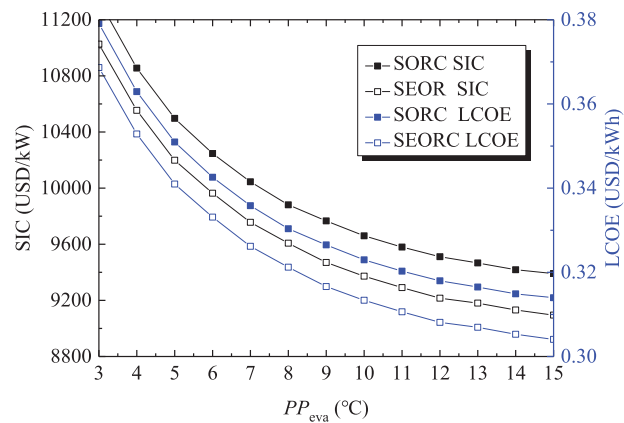


Figure 12: Variations of SIC and LCOE with evaporator pinch point temperature difference

5.5 Effects of Condenser Pinch Point Temperature Difference

The influences of PP_{con} on the on the SORC and SEORC system performance are charted in Figs. 13 and 14. It is observed that, in accordance with expectations, for both SORC and SEORC, the η_{th} and η_{ex} exhibit a linear decline as PP_{con} increases, which is attributable to the rise in condensation temperature. The PP_{con} has larger impact on the η_{th} and η_{ex} of SEORC than those of SORC. While the SIC and LCOE both exhibit an initial reduction followed by an increase as PP_{con} rises. At a PP_{con} of 10°C, the SIC and LCOE reach the minimum values. The rationale behind this trend is analogous to that of PP_{con} , while the PP_{con} has different effect degree on the total input heat and heat exchanger area. Relative to PP_{eva} , the PP_{con} yields a more pronounced effect on η_{th} and η_{ex} .

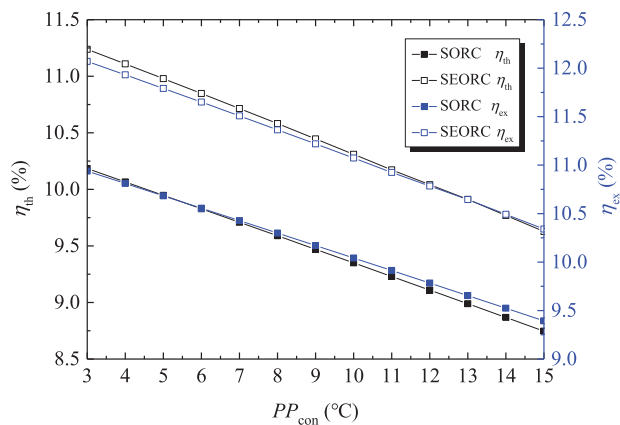


Figure 13: Variations of thermal efficiency and exergy efficiency with condenser pinch point temperature difference

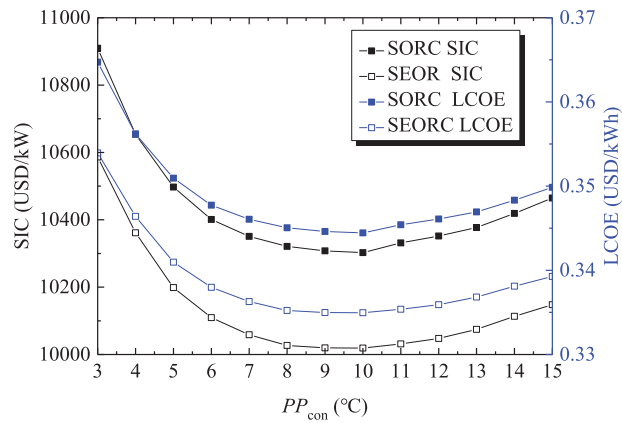


Figure 14: Variations of SIC and LCOE with condenser pinch point temperature difference

6 Conclusions

In the present study, a vapor-liquid ejector has been integrated into the PTC-driven ORC system to reduce the working fluid pump power consumption and to alleviate turbine backpressure. A detailed thermo-economic model has been developed. The thermodynamic and economic comparison between the SORC and SEORC are conducted. The study also explores the effects of solar beam radiation intensity, PTC temperature drop, evaporator pinch point temperature difference, and condenser pinch point temperature difference on thermal efficiency, exergy efficiency, specific investment cost, and levelized cost of energy. The conclusions drawn are as follows:

(1) The SEORC consistently demonstrates superior thermo-economic performance compared to the SORC, particularly when the working fluid pump exhibits lower isentropic efficiency. At a solar beam radiation intensity of $1000\text{W}/\text{m}^2$, the SEORC's η_{th} and η_{ex} are 1.08 and 1.08 times as large as those of the SORC. An increase in solar beam radiation intensity enhances system performance.

(2) There is an optimal ΔT at which η_{th} and η_{ex} achieves the maximum. At higher ΔT values, the SEORC shows greater superiority over the ORC. At a ΔT of 50°C , the η_{th} of SEORC is 1.17 times larger than that of ORC. Similarly, at a ΔT of 50°C , the SIC and LCOE for the SEORC decrease by 6.3% compared to the SORC.

(3) An increase in T_{in} is conducive to the system thermo-economic performance. With high T_{in} , the SEORC is more excellent than the SORC. The T_{in} has a more profound impact on thermodynamic performance than on economic performance.

(4) A rise in PP_{eva} will reduce the η_{th} and η_{ex} of the SORC and SEORC. However, this increase in PP_{eva} concurrently leads to a reduction in the required heat exchanger area, which in turn enhances the SIC and LCOE. When PP_{eva} exceeds 12°C , the PP_{eva} has minor impact on SIC and LCOE. In other words, the PP_{eva} should not exceed 12°C under the working conditions considered in this study.

(5) In contrast to PP_{eva} , PP_{con} has different influence on the system performance. A higher PP_{con} leads to lower η_{th} and η_{ex} . When the PP_{con} is 10°C , the SIC and LCOE reach the minimum values. Compared to PP_{eva} , the PP_{con} has a more significant impact on the η_{th} and η_{ex} .

Acknowledgement: Not applicable.

Funding Statement: This research was funded by Natural Science Foundation of Guangdong Province, grant number 2024A1515030130, and National Natural Science Foundation of China, grant number 42102336.

Author Contributions: Conceptualization, Lingbao Wang and Zuowei Yang; methodology, Lingbao Wang and Zuowei Yang; software, Zhi Gan and Huashan Li; validation, Zhi Gan and Huashan Li; formal analysis, Yulie Gong and Xianbiao Bu; investigation, Huashan Li; resources, Xianbiao Bu; data curation, Zhi Gan; writing—original draft preparation, Lingbao Wang; writing—review and editing, Xianbiao Bu; visualization, Yulie Gong; supervision, Zuowei Yang; project administration, Yulie Gong; funding acquisition, Lingbao Wang. All authors reviewed the results and approved the final version of the manuscript.

Availability of Data and Materials: The data that support the findings of this study are available from the corresponding author, Yang Z.W., upon reasonable request.

Ethics Approval: Not applicable.

Conflicts of Interest: The authors declare no conflicts of interest to report regarding the present study.

Nomenclature

Symbols

A	Heat exchanger area (m^2)
C	Investment cost (USD)
c_1	Sound velocity (m/s)
c_p	Specific heat capacity ($\text{kJ/kg}\cdot\text{K}^{-1}$)
E	Available solar exergy (kW)
G_b	Solar beam radiation intensity (W/m^2)
h	Specific enthalpy (kJ/kg)
i	Annual loan interest rate
I	Irreversible loss, kW
KA	Thermal conductivity rate, W/K
m	Mass flow rate (kg/s)
Ma	Mach number
P	Pressure (kPa)
Q	Heat transfer rate (kW)
R	Section area ratio
S	Entropy generation (kW/K)
T	Temperature ($^{\circ}\text{C}$)
U	Flow velocity (m/s)
VF	Fraction dryness of mixed working fluid
W	Work (kW)
x	Dryness of the working fluid
ΔT	Logarithmic temperature difference ($^{\circ}\text{C}$)

Greek

η	Efficiency
k	Heat capacity ratio
λ	Coefficient of thermal conductivity ($\text{W}/(\text{m}\cdot\text{K})$)
ρ	Density (kg/m^3)
μ	Viscosity (Pa·s)
ε	Efficiency

Subscripts

0	Ambient condition
1, 2, . . . , 12	State points
am	Ambient

ava	Available
ave	Average
cw	Cooling water
c	Condenser
col	Parabolic trough collector
e	Evaporator
ex	Exergy
hx	Heat exchanger
in	Inlet
net	Net power output
out	Outlet
p	Working fluid pump
s	Isentropic process
syl	Syltherm 800
t	Turbine
tot	Total
th	Thermal
u	Useful
wf	Working fluid

Acronyms

CEPCI	Chemical engineering plant cost index
CRF	Capital recovery factor
GWP	Global warming potential
EORC	Ejector organic Rankine cycle
ODP	Ozone depletion potential
PTC	Parabolic trough collector
SIC	Specific investment cost

References

1. Sufyanullah K, Ahmad KA, Ali MAS. Does emission of carbon dioxide is impacted by urbanization? An empirical study of urbanization, energy consumption, economic growth and carbon emissions—using ARDL bound testing approach. *Ener Poli.* 2022;164:112908. doi:10.1016/j.enpol.2022.112908.
2. Zhao X, Ma X, Chen B, Shang Y, Song M. Challenges toward carbon neutrality in China: strategies and counter measures. *Resourc Conservat Recycl.* 2022;176:105959. doi:10.1016/j.resconrec.2021.105959.
3. Obaideen K, AlMallahi MN, Alami AH, Ramadan M, Abdelkareem MA, Shehata N, et al. On the contribution of solar energy to sustainable developments goals: case study on Mohammed bin Rashid Al Maktoum Solar Park. *Int J Thermofluids.* 2021;12:100123. doi:10.1016/j.ijft.2021.100123.
4. Fan G, Song J, Zhang J, Fu Z, Gong X, Dai Y, et al. Thermo-economic assessment and systematic comparison of combined supercritical CO₂ and organic Rankine cycle (SCO₂-ORC) systems for solar power tower plants. *Appl Therm Eng.* 2024;236:121715. doi:10.1016/j.applthermaleng.2023.121715.
5. Gharat PV, Bhalekar SS, Dalvi VH, Panse SV, Deshmukh SP, Joshi JB. Chronological development of innovations in reflector systems of parabolic trough solar collector (PTC)—a review. *Renew Sustain Energy Rev.* 2021;145:111002. doi:10.1016/j.rser.2021.111002.
6. Rayegan R, Tao YX. A procedure to select working fluids for Solar Organic Rankine Cycles (ORCs). *Renew Energy.* 2011;36(2):659–70. doi:10.1016/j.renene.2010.07.010.
7. Desai NB, Bandyopadhyay S. Thermo-economic analysis and selection of working fluid for solar organic Rankine cycle. *Appl Therm Eng.* 2016;95(7):471–81. doi:10.1016/j.applthermaleng.2015.11.018.

8. Soulis KX, Manolakos D, Ntavou E, Kosmadakis G. A geospatial analysis approach for the operational assessment of solar ORC systems: case study—performance evaluation of a two-stage solar ORC engine in Greece. *Renew Energy*. 2022;181:116–28. doi:10.1016/j.renene.2021.09.046.
9. Calise F, Capuozzo C, Carotenuto A, Vanoli L. Thermoeconomic analysis and off-design performance of an organic Rankine cycle powered by medium-temperature heat sources. *Sol Energy*. 2014;103:595–609. doi:10.1016/j.solener.2013.09.031.
10. Roumpedakis TC, Loumpardis G, Monokrousou E, Braimakis K, Charalampidis A, Karellas S. Exergetic and economic analysis of a solar driven small scale ORC. *Renew Energy*. 2020;157:1008–24. doi:10.1016/j.renene.2020.05.016.
11. Georgousis N, Lykas P, Bellos E, Tzivanidis C. Multi-objective optimization of a solar-driven polygeneration system based on CO₂ working fluid. *Energy Convers Manag*. 2022;252:115136. doi:10.1016/j.enconman.2021.115136.
12. Javed S, Tiwari AK. Performance assessment of different Organic Rankine Cycle (ORC) configurations driven by solar energy. *Process Saf Environ Prot*. 2023;171:655–66. doi:10.1016/j.psep.2023.01.039.
13. Freeman J, Hellgardt K, Markides CN. An assessment of solar-powered organic Rankine cycle systems for combined heating and power in UK domestic applications. *Appl Energy*. 2015;138:605–20. doi:10.1016/j.apenergy.2014.10.035.
14. Bellos E, Tzivanidis C. Parametric analysis and optimization of a solar driven trigeneration system based on ORC and absorption heat pump. *J Clean Prod*. 2017;161:493–509. doi:10.1016/j.jclepro.2017.05.159.
15. Jafary S, Khalilarya S, Shawabkeh A, Wae-hayee M, Hashemian M. A complete energetic and exergetic analysis of a solar powered trigeneration system with two novel organic Rankine cycle (ORC) configurations. *J Clean Prod*. 2021;281:124552. doi:10.1016/j.jclepro.2020.124552.
16. Giménez-Prades P, Navarro-Esbri J, Arpagaus C, Fernández-Moreno A, Mota-Babiloni A. Novel molecules as working fluids for refrigeration, heat pump, and organic Rankine cycle systems. *Renew Sustain Energy Rev*. 2022;167(12):112549. doi:10.1016/j.rser.2022.112549.
17. Krail J, Beckmann G, Schittl F, Piringner G. Comparative thermodynamic analysis of an improved ORC process with integrated injection of process fluid. *Energy*. 2023;266:126352. doi:10.1016/j.energy.2022.126352.
18. Tahir MBINM, Yamada N. Characteristics of small ORC system for low-temperature waste heat recovery. *J Environ Eng*. 2009;4(2):375–85. doi:10.1299/jee.4.375.
19. Quoilin S, Van Den Broek M, Declaye S, Dewallef P, Lemort V. Techno-economic survey of organic Rankine cycle (ORC) systems. *Renew Sustain Energy Rev*. 2013;22(3):168–86. doi:10.1016/j.rser.2013.01.028.
20. Zhang X, Zhang Y, Wang J. Evaluation and selection of dry and isentropic working fluids based on their pump performance in small-scale organic Rankine cycle. *Appl Therm Eng*. 2021;191:116919. doi:10.1016/j.applthermaleng.2021.116919.
21. Jiang L, Lu HT, Wang LW, Gao P, Zhu FQ, Wang RZ, et al. Investigation on a small-scale pumpless Organic Rankine Cycle (ORC) system driven by the low-temperature heat source. *Appl Energy*. 2017;195(1):478–86. doi:10.1016/j.apenergy.2017.03.082.
22. Yang Y, Zhang H, Xu Y, Yang F, Wu Y, Lei B. Matching and operating characteristics of working fluid pumps with organic Rankine cycle system. *Appl Therm Eng*. 2018;142(21):622–31. doi:10.1016/j.applthermaleng.2018.07.039.
23. Doninelli M, Di Marcoberardino G, Iora P, Gelfi M, Invernizzi CM, Manzolini G. Silicon Tetrachloride as innovative working fluid for high-temperature Rankine cycles: thermal stability, material compatibility, and energy analysis. *Appl Therm Eng*. 2024;249:123239. doi:10.1016/j.applthermaleng.2024.123239.
24. Saadon S, Mohd Nasir NA. Performance and sustainability analysis of an organic Rankine cycle system in subcritical and supercritical conditions for waste heat recovery. *Energies*. 2020;13(12):3035. doi:10.3390/en13123035.
25. Wang Y, Song J, Chatzopoulou MA, Sunny N, Simpson MC, Wang J, et al. A holistic thermoeconomic assessment of small-scale, distributed solar organic Rankine cycle (ORC) systems: comprehensive comparison of configurations, component, and working fluid selection. *Energy Convers Manag*. 2021;248(5):114618. doi:10.1016/j.enconman.2021.114618.
26. Haghparast P, Sorin MV, Richard MA, Nesreddine N. Analysis and design optimization of an ejector integrated into an organic Rankine cycle. *Appl Therm Eng*. 2019;159(4):113979. doi:10.1016/j.applthermaleng.2019.113979.

27. Sanaye S, Refahi A. A novel configuration of ejector refrigeration cycle coupled with organic Rankine cycle for transformer and space cooling applications. *Int J Refrig.* 2020;115(6):191–208. doi:10.1016/j.ijrefrig.2020.02.005.
28. Loni R, Mahian O, Markides CN, Bellos E, Le Roux WG, Kasaeian A, et al. A review of solar-driven organic Rankine cycles: recent challenges and future outlook. *Renew Sustain Energ Rev.* 2021;150:111410. doi:10.1016/j.rser.2021.111410.
29. Wang S, Liu C, Li Q, Liu L, Huo E, Zhang C. Selection principle of working fluid for organic Rankine cycle based on environmental benefits and economic performance. *Appl Therm Eng.* 2020;178:115598. doi:10.1016/j.applthermaleng.2020.115598.
30. Bell IH, Wronski J, Quoilin S, Lemort V. Pure and pseudo-pure fluid thermophysical property evaluation and the open-source thermophysical property library CoolProp. *Indust Eng Chem Res.* 2014;53(6):2498–508. doi:10.1021/ie4033999.
31. Kalogirou SA. Solar thermal collectors and applications. *Prog Energy Combust Sci.* 2004;30:231–95. doi:10.1016/j.pecs.2004.02.001.
32. Dudley VE, Evans LR, Matthews CW. Test results, industrial solar technology parabolic trough solar collector (SAND94-1117). Albuquerque, NM, USA: Sandia National Laboratory; 1995.
33. Yan YJ, Shao SF, Liu JP, Zhang Z. Experiment and analysis on performance of steam-driven jet injector for district-heating system. *Appl Therm Eng.* 2005;25(8–9):1153–67. doi:10.1016/j.applthermaleng.2004.09.001.
34. Chen Z, Liu G, Zhao H, Deng J. Analysis of the internal flow features of a CO₂ transonic nozzle and optimization of the nozzle shape profile. *Appl Therm Eng.* 2024;238:121945. doi:10.1016/j.applthermaleng.2023.121945.
35. Chen JY, Havtun H, Palm B. Investigation of ejectors in refrigeration system: optimum performance evaluation and ejector area ratios perspectives. *Appl Therm Eng.* 2014;64(1–2):182–91. doi:10.1016/j.applthermaleng.2013.12.034.
36. Chen JY, Huang YS, Niu ZT, Luo XL, Chen Y, Yang Z. Investigation of vapor-liquid ejector with organic working fluids. *J Therm Sci.* 2019;28(01):61–71. doi:10.1007/s11630-018-1031-2.
37. Chen T, Kim J, Cho H. Theoretical analysis of the thermal performance of a plate heat exchanger at various chevron angles using lithium bromide solution with nanofluid. *Int J Refrig.* 2014;48(01):233–44. doi:10.1016/j.ijrefrig.2014.08.013.
38. Han D-H, Lee K-J, Kim Y-H. Experiments on the characteristics of evaporation of R410A in brazed plate heat exchangers with different geometric configurations. *Appl Therm Eng.* 2003;23(10):1209–25. doi:10.1016/S1359-4311(03)00061-9.
39. Longo GA, Righetti G, Zilio C. A new computational procedure for refrigerant condensation inside herringbone-type Brazed Plate Heat Exchangers. *Int J Heat Mass Transf.* 2015;82(541–546):530–6. doi:10.1016/j.ijheatmasstransfer.2014.11.032.
40. Yang MH, Yeh RH. Economic performances optimization of the transcritical Rankine cycle systems in geothermal application. *Energy Convers Manag.* 2015;95:20–31. doi:10.1016/j.enconman.2015.02.021.
41. Hashemi M, Jenkins G, Milne F. Rooftop solar with net metering: an integrated investment appraisal. *Renew Sustain Energ Rev.* 2023;188(3):113803. doi:10.1016/j.rser.2023.113803.
42. Kocaman E, Karakuş C, Yağlı H, Koç Y, Yumrutaş R, Koç A. Pinch point determination and multi-objective optimization for working parameters of an ORC by using numerical analyses optimization method. *Energy Convers Manag.* 2022;271:116301. doi:10.1016/j.enconman.2022.116301.
43. Ding X, Yang L, Zheng N, Duan L, Zhou Y. Dynamic response characteristics and economic analyses of two solar-assisted multi-generation systems. *Appl Therm Eng.* 2024;241:122339. doi:10.1016/j.applthermaleng.2024.122339.
44. Li TL, Zhu JL, Zhang W. Cascade utilization of low temperature geothermal water in oilfield combined power generation, gathering heat tracing and oil recovery. *Appl Therm Eng.* 2005;40(2012):27–35. doi:10.1016/j.applthermaleng.2012.01.049.
45. Krempus D, Bahamonde S, van der Stelt TP, Klink W, Colonna P, De Servi CM. On mixtures as working fluids of air-cooled ORC bottoming power plants of gas turbines. *Appl Therm Eng.* 2024;236(6):121730. doi:10.1016/j.applthermaleng.2023.121730.